ELSEVIER

Journal of the Mechanics and Physics of Solids
51 (2003) 2085–2104

JOURNAL OF THE
MECHANICS AND
PHYSICS OF SOLIDS

www.elsevier.com/locate/jmps

Nanoindentation effect on the optical properties of self-assembled quantum dots

H.T. Johnson*, R. Bose

Department of Mechanical and Industrial Engineering, University of Illinois at Urbana-Champaign, Urbana, IL 61801, USA

Abstract

The optical emission spectrum of a quantum dot array is computed for a series of cases in which a nanometer scale microscope tip indenter is used to impose increasing elastic strain on the sample. The system under consideration consists of approximately 30 self-assembled $In_{0.55}Al_{0.45}As$ quantum dots buried in a matrix material of $Al_{0.35}Ga_{0.65}As$; the indenter is a tapered optical fiber tip used to collect emitted light from the array while simultaneously imposing strain on the sample. A continuum analysis is used to compute the confined electron and hole energies and wave functions in the presence of the imposed elastic indentation strain field. The analysis includes the consideration of exciton binding energy effects, which are found to be small for quantum dots in the size range of interest. From the computed energy states, the optical conductivity of the system is evaluated using simple scattering rate theory. The blue-shift in light emitted by individual dots predicted by the analysis agrees well with experimental observations by Robinson et al. (Appl. Phys. Lett. 72 (1998) 2081). Finally, a simple dislocation nucleation estimate based on a Rice–Thomson-type analysis is developed for the system. The estimate supports the observation that dislocation activity in the single crystalline sample may be responsible for the experimentally observed optical emission quenching when indentation exceeds a critical depth.

Keywords: A. Dislocations; A. Electromechanical processes; B. Semiconductor material; C. Finite elements; C. Optical microscopy

1. Introduction

Nanometer scale semiconductor structures are of increasing interest for a variety of electronic and optical applications. Quantum dots, or nanometer scale structures

* Corresponding author. Tel.: +1-217-265-5468; fax: +1-217-244-6534.
E-mail address: htj@uiuc.edu (H.T. Johnson).

0022-5096/$ - see front matter © 2003 Elsevier Ltd. All rights reserved.
doi:10.1016/j.jmps.2003.09.020

used to quantum mechanically confine charge carriers, are used as photo-detectors and emitters in low threshold-current lasers (Bimberg et al., 1999, and references contained therein), as well as more recently for nano-biological devices (Winter et al., 2001) and quantum computing elements (Biolatti et al., 2000). Semiconductor quantum dots are fabricated either through "top-down" approaches based on lithographic methods, or through "bottom-up" self-assembly based approaches (Leon et al., 1995). Self-assembly is a convenient route to large ensembles or arrays of dots, but control over size, shape, and spatial regularity is problematic. For this reason, characterization and modeling methods must be capable of resolving both individual dot features and small groups of dots in which collective effects and properties can be observed.

Self-assembled quantum dots are grown by heteroepitaxial deposition methods, free of defects, and with perfectly coherent bimaterial interfaces. Dislocations have deleterious electrical effects and are avoided by design, but elastic strain due to lattice mismatch is often as large as several percent. It may vary dramatically over lengths as small as several nanometers because of free surfaces, interfaces, and other sharply defined geometrical features, and it strongly affects electrical and optical properties of the devices. Numerous investigators report on this effect; Johnson and Freund (2001) formulate the continuum mechanics theory of strain effects on quantum confinement in semiconductor heterostructures.

Interest in semiconductor nanostructures is increasingly driven by advances in experimental characterization methods, which allow for atomic scale imaging resolution and optical spectral measurements at length scales far below the wavelength of visible light. Near-field scanning optical microscopy (NSOM), for example, is used to excite or collect near-infrared emitted light from small groups of nanometer scale quantum dots and is able to resolve the emission characteristics of individual dots (Robinson et al., 1998; Robinson et al., 2001). The microscope tip used in NSOM is a tapered optical fiber with a flat aperture having a diameter much smaller than a micron.

Compelling recent NSOM measurements by Robinson et al. (1998) on self-assembled quantum dot arrays are considered in the present work. In this study, Robinson and co-workers use an NSOM tip with a 250 nm wide flat aperture to collect emitted light from a self-assembled quantum dot array while simultaneously imposing an elastic strain by indenting the sample with the tip. The effect of the externally imposed strain is to increase (decrease) the energy (wavelength) of the light emitted from individual dots in the array. Simple estimates by Robinson and co-workers ascribe the direction of the shift to the influence of strain, but the prediction yields a shift more than an order of magnitude larger than observed in the experiment. The estimate reported by Robinson et al. (1998) also predicts a uniform strain shift from dot to dot in the sample. The experiment shows, however, that for indentation depths larger than a particular value, some quantum dots cease to emit light while others continue to exhibit the strain-related blue shift in emitted light.

In the present work, the problem of indentation on an array of buried self-assembled quantum dots is considered. The approach is to incorporate the full strain field due to indentation by a rigid cylindrical indenter into the quantum mechanical analysis that yields an optical spectrum for the sample. Material properties are chosen to represent the system measured by Robinson et al. (1998), although the geometrical details

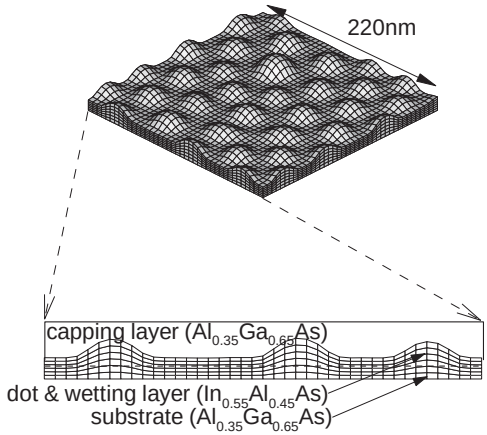

Fig. 1. Finite element mesh and schematic of the quantum dot system under consideration. The substrate and capping layer (elements omitted for clarity) are composed of $Al_{0.35}Ga_{0.65}As$, while the quantum dots and wetting layer are $In_{0.65}Al_{0.45}As$. Typical dot diameters are approximately 20 nm.

of the quantum dot array are taken from results of previous morphological studies by Zhang and Bower (1999). The particular sample under consideration is shown in Fig. 1. An effort is made to correctly account for the relationship between measured compression in the experimental work and the actual indentation depth, which partially accounts for the initial overestimate of the strain induced optical shift by Robinson et al. (1998). Accounting for the full strain tensor field further increases the accuracy of the prediction to within a factor of order one. The present work also considers some other features of the quantum dot array problem, such as the effect of exciton binding energy, or the Coulombic attraction between the electron/hole pair responsible for optical emission. This effect is found to be significant for computed optical spectra in atomistic analyses (Zunger, 2001), but here it is shown to be small due to the realistic size of the quantum dots under consideration. Finally, a simple estimate based on a Rice–Thomson-type analysis yields an approximate indentation depth at which a dislocation would be expected to nucleate in the quantum dot sample. This estimate, combined with an analysis of the electrostatic perturbation due to an electrically active dislocation, justifies the premise that dislocation activity may be responsible for the observed optical emission quenching at large indentation depths.

2. Electron confinement and optical spectra in self-assembled quantum dot arrays

To compute the optical emission and absorption spectra for a semiconductor quantum structure such as an array of quantum dots, electron and hole energy levels and wave functions are needed. The approach taken here is to consider the energetics of a single, additional charge carrier in a continuum approximation, in which the conduction and valence electrons intrinsic to the material are treated in an average sense using an

effective potential. The ballistic charge carrier is assigned a tensor effective mass, which describes the dynamics of the carrier when subjected to an applied electric field. The effective mass tensor bears the symmetry of the underlying crystal structure which may be elastically strained, but which is assumed to be free of defects. The approach is described in detail from a mechanics perspective by Johnson and Freund (2001), and has been used by others (Jiang and Singh, 1997; Johnson et al., 1998; Pryor, 1998, for example) to describe a variety of quantum semiconductor devices. The form of the Hamiltonian describing the behavior of the single charge carrier is given by Luttinger and Kohn (Singh, 1993) and is derived from $\mathbf{k}\cdot\mathbf{p}$ theory.

Within this framework, the single charge carrier behaves according to the Schrodinger equation, written as

$$-\frac{\hbar^2}{2m}\nabla_i L_{ij}^{\alpha\beta}\nabla_j \Psi^\beta + V^{\alpha\beta}\Psi^\beta = -i\hbar\frac{\partial\psi^\alpha}{\partial t}, \tag{1}$$

where Ψ is the wave function of the carrier, V is the spatially varying potential field through which the charge carrier does work, and L is the Luttinger–Kohn Hamiltonian containing the effective mass tensor parameters. The indices α and β represent the energy subbands that form a basis for the wave function of the charge carrier; this basis may include 1, 2, 4, 8, or more subbands within the conduction and valence bands of the material. A larger subband basis increases the energy accuracy of the calculation (Pryor, 1998a) but at a computational cost on the order of the number of subbands squared. The results shown here are obtained in the single subband (tensor effective mass) approximation, where the energy levels of the conduction electrons and valence electrons are computed separately. The modal dynamics of an electron or hole are governed by the solutions to the steady-state form, or

$$-\frac{\hbar^2}{2m}\nabla_i L_{ij}^{\alpha\beta}\nabla_j \Psi^\beta + V^{\alpha\beta}\Psi^\beta = E\Psi^\alpha. \tag{2}$$

The potential field V is input to the calculation based on the local composition of the material and the local state of strain in the material. Other possible contributions to V, not considered here, include an applied electric potential or a piezoelectric potential. Thus, V can be written as

$$V^{\alpha\beta} = V_{\text{comp}}^{\alpha\beta} + V_{\text{strain}}^{\alpha\beta}, \tag{3}$$

where the compositional contribution of the potential is due to the energy band misalignment between adjacent layers (e.g. dot layer/capping layer) in the heterostructure. This contribution ranges from 0.1 to 1.5 eV depending on the layer compositions and the subbands under consideration. The strain portion of the potential couples the elasticity problem to the quantum mechanical behavior of the charge carrier under consideration. This coupling is quantified through deformation potential theory, which converts an elastic strain ε_{ij} into an electrostatic potential $V_{\text{strain}}^{\alpha\beta}$ through the scalar product given by

$$V_{\text{strain}}^{\alpha\beta} = D_{ij}^{\alpha\beta}\varepsilon_{ij}, \tag{4}$$

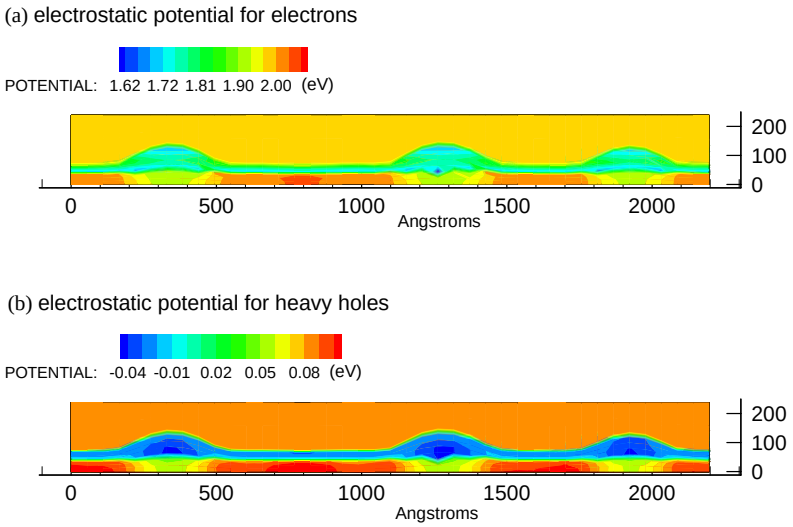

Fig. 2. Confining electrostatic potential for (a) electrons and (b) heavy holes for the un-indented quantum dot array. The heavy hole confining energy is much shallower than the electron confining energy. Both cases show strong strain sensitivity, including regions of strain-enhanced confinement within the individual quantum dots.

where $D_{ij}^{\alpha\beta}$ is the deformation potential tensor field in the material, a local material property. The components of the deformation potential tensor have values on the order of 1–10 eV. Thus, depending on local composition and strain, the elastic contribution may approach the magnitude of the compositional contribution to the electrostatic potential. A potential profile for an array of quantum dots with only the effects of material composition and elastic mismatch strain is shown in Fig. 2.

Material inputs to the electron/hole modal analysis include the effective mass tensor components of the charge carriers, and the deformation potential tensor components for the material. The potential field V is computed from the elastic strain which until now includes only the mismatch strain associated with the deposition and assembly process. The mismatch elastic strain field is obtained from the same analysis (Zhang and Bower, 1999) that gives the initial quantum dot morphology configuration. The material constants (masses and deformation potentials) used in the calculations described here are listed in Table 1. The table lists the Luttinger–Kohn parameters, from which the effective mass tensor components are obtained, and the deformation potentials, from which the conduction and heavy hole bandedge shifts are obtained.

From these properties, and a quantum dot array configuration such as the ensemble shown in Fig. 1 (with elements added to model a suitable capping layer), the modes or energy states for the electrons and holes are computed. Eq. (2) is solved using a standard Galerkin finite element method described in detail by Johnson and Freund (2001). The lowest lying energy states represent the most tightly confined electrons or holes; these states dominate the optical spectra in the energy range of interest. Previous

Table 1
Input properties for electronic confinement calculation

Property	Barrier: $Al_{0.35}Ga_{0.65}As$	Well: $In_{0.55}Al_{0.45}As$
Bandgap (eV)	2.08	1.63
Luttinger–Kohn		
Effective mass parameters:		
m_e	0.0961	0.080
γ_1	5.63	12.77
γ_2	1.47	4.87
γ_3	2.23	5.59
$m_{hh,x} = 1/(\gamma_1 + \gamma_2)$		
$m_{hh,z} = 1/(\gamma_1 - 2\gamma_2)$		
Deformation potentials (eV)		
a_c	−6.635	−5.332
a_v	1.619	1.662
b	−1.630	−1.665
$\delta E_c = a_c(\varepsilon_{xx} + \varepsilon_{yy} + \varepsilon_{zz})$		
$\delta E_{hh} = a_v(\varepsilon_{xx} + \varepsilon_{yy} + \varepsilon_{zz}) + (b/2)(\varepsilon_{xx} + \varepsilon_{yy} - 2\varepsilon_{zz})$		

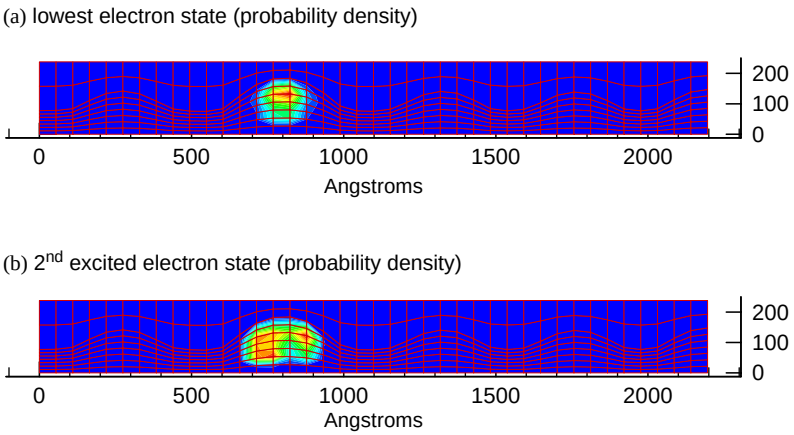

Fig. 3. Cross-sectional views of low energy confined electron states in the un-indented quantum dot array. (a) The lowest energy or ground state shows spherical or s-type symmetry in the probability density distribution; (b) The second excited state shows two-fold or p-type symmetry in the plane of the quantum dot array. Higher energy states (not shown) include energy levels that are delocalized and split between multiple dots.

investigators compute energy levels in a similar manner for individual quantum dots; here, the spectrum of states includes localized modes for all dots in the array as well as extended modes that couple multiple dots in the array. Fig. 3 shows two representative low-energy (tightly confined) states. Delocalized states generally occur

at energies outside the range of interest here. These states are used to explain various fine structure and resonances in the optical spectra of the systems (Johnson et al., 2003).

Optical properties are obtained from the computed energy levels for electrons and holes in the quantum dot array. The connection between charge carrier spectra and optical spectrum is made by considering the optical conductivity of the system. The real part of the optical conductivity, or the optical absorption, exhibits special frequencies at which absorption (and therefore emission) is most highly effective. These frequencies are found by constructing the relative interband absorption spectrum according to (Davies, 1998)

$$\sigma_1(\omega) = \frac{2\pi}{\Omega\omega}\left(\frac{e}{m_0}\right)^2 \sum_{i,j} |\mathbf{e}\cdot\mathbf{p}_{i,j}|^2 |\langle i|j\rangle|^2 \delta(E_i - E_j - \hbar\omega). \tag{5}$$

The constants Ω, or volume of the system, electron charge e, and mass m_0, do not affect the relative absorption over the narrow range of frequencies ω of interest. The first term in the summation over conduction and valence states i and j is constant for fixed energy subbands, taken here to be the conduction electrons and the heavy holes, transitions between which dominate the spectrum. This part of the optical matrix element represents the scalar product between the polarization vector of the incident light and the momentum vector of the charge carrier. The second squared term in the summation represents the spatial overlap integral between the wave function of states i and j. This part of the matrix element determines the relative intensity of light emitted or absorbed through a transition between states i and j. The final Dirac delta function term matches the energy of the emitted or absorbed light, $\hbar\omega$, to the energy difference between states i and j. The overlap and delta function terms reduce in a first approximation to the so-called $\Delta n = 0$ rule, which holds that the dominant transitions for a single potential well (quantum dot) are due to pairs of the ground electron/hole states, first excited electron/hole states, second excited electron/hole states, etc. Fig. 4 shows a one-dimensional schematic of the transition process between electrons and holes responsible for emission or absorption. This type of analysis for quantum dot arrays is first described by Johnson et al. (2002).

From this analysis, an optical emission/absorption spectrum is readily generated. The overlap integral term, which determines the strength of the transition between two electron and hole states i and j, is represented graphically in an overlap diagram of the kind shown in Fig. 5. In this plot, the intensity of each possible transition in the system is shown in color at the point corresponding to the electron and hole energy involved in the transition. Organized in this way, the plot shows clear groups of transitions for the array, such as transitions between s-type electrons and s-type holes, which appear as a diagonal streak closest to the origin of the plot. Confinement is strongest for the lowest energy states, so overlap values between electrons and holes tend to be largest near the origin. At higher energies there is more disorder in the plot, as states are less strongly confined; near-degeneracy between multiple states leads to additional weak transitions. At the highest energies considered here, the heavy holes are essentially delocalized and approach wetting layer states, so all structure in the overlap diagram is lost. An important additional feature of the plot is that horizontal

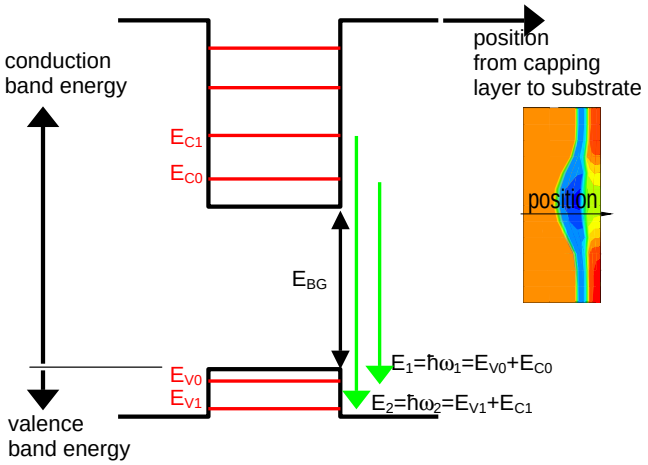

Fig. 4. One-dimensional schematic of the band structure connection to optical transition energies. The orientation of the position dimension relative to the quantum dot layer is shown inset. The computed energy levels for electrons and holes (represented as horizontal lines) are used to predict the transition energies (represented as vertical arrows on the right). The arbitrary zero in energy is chosen here to coincide with the quantum well valence band edge.

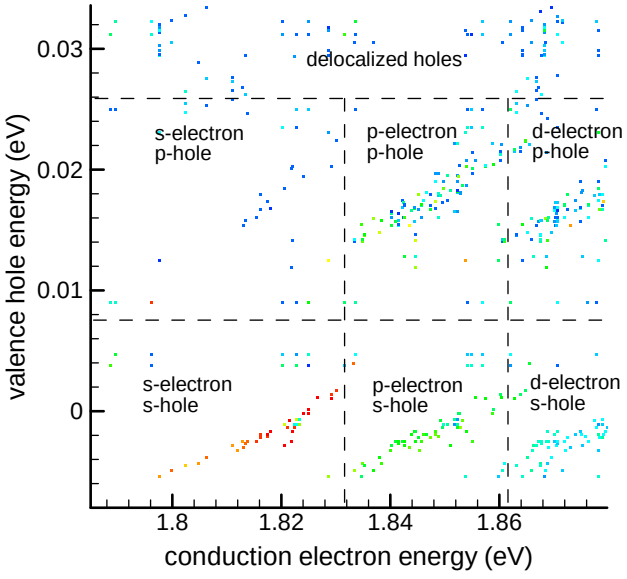

Fig. 5. Overlap diagram between electrons and heavy holes in the un-indented quantum dot array. Color of each point represents the relative intensity of the spatial overlap or transition between the states. Dashed lines separate diagonal streaks representing overlap between symmetry-based groups of states. There is less structure at higher energies, particularly for the less strongly confined heavy holes.

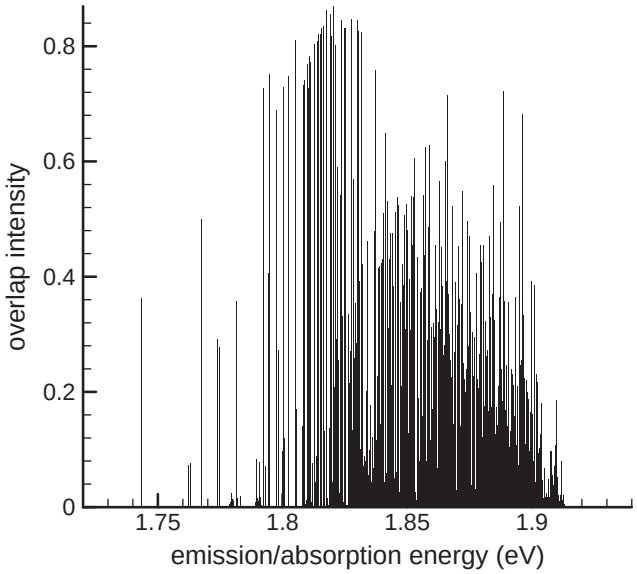

Fig. 6. Simulated emission/absorption spectrum for the un-indented array. The spectrum is comparable to experimental PL and PLE spectra. The range of energies is due to inhomogeneous broadening typical of experimentally measured quantum dot ensembles.

(vertical) streaks represent overlap between a single delocalized hole (electron) state and multiple localized electron (hole) states. This observation is related to excitation resonances in the experimentally measured optical spectrum (Johnson et al., 2003).

The overlap diagram is expanded along a single energy axis to represent an emission/absorption spectrum, shown in Fig. 6, that is comparable to experimental photoluminescence (PL) and photoluminescence excitation (PLE) spectra. Each line represents a single optical transition in the system, with a spread of energies due to the variation in size of the dots in the array. The energy of each line is obtained by summing the electron and hole energies for transitions that appear in the overlap diagram. The main two groups of transitions that form the spectrum are due to s/s-type electron/hole pairs and p/s-type electron/hole pairs.

3. Exciton energies for self-assembled quantum dots

The exciton binding energy is a significant correction to the $\mathbf{k} \cdot \mathbf{p}$ Hamiltonian or effective mass method of computing energies for optical transitions. The exciton energy is due to the electrostatic energy gain resulting from the attraction between the electron and hole pair responsible for the optical transition. Zunger (2001) and others use atomistic electronic structure methods to extensively study exciton energies and higher order corrections due to exchange correlation energies. Atomistic methods such as the empirical pseudopotential approach find that effects are significant in smaller quantum

Table 2
Exciton energies for a sample of representative quantum dots

Dot	0 nm sample displacement (meV)	20 nm sample displacement (meV)
1	5.6	5.6
2	6.0	6.0
3	5.9	6.1
4	6.3	6.3
5	6.1	6.2
6	6.2	6.2
Mean	6.0	6.1

dots (with $d < 5$ nm, for example). The analyses suggest that larger dots will show smaller effects. However, these methods are prohibitively computationally intensive for the realistic large dots considered here (with $d > 10$ nm, for example). For systems of this size, the accepted approach is to evaluate integrals over the envelope wave functions directly, as done by Grundmann et al. (1995).

Within this continuum approach, for an electron–hole pair described by wave functions Ψ_e and Ψ_h, the exciton binding energy is given by

$$E_{\text{Coul}} = \frac{e^2}{4\pi\varepsilon_0\varepsilon_r} \int\int \frac{|\Psi_h(\mathbf{r}_h)|^2 |\Psi_e(\mathbf{r}_e)|^2}{|\mathbf{r}_h - \mathbf{r}_e|} \, d^3\mathbf{r}_h \, d^3\mathbf{r}_e, \tag{6}$$

where $\mathbf{r}_e$ and $\mathbf{r}_h$ are position vectors describing the corresponding wave functions, e is the electron charge, and ε_0 and ε_r are the permittivity of free space and the dielectric constant of the material, respectively. The integral ranges over volume, but the wave functions decay exponentially outside of the individual quantum dot in which the states are confined. Based on the energy states obtained as described in the previous section, it is straightforward to evaluate the integral for all dots of interest. Typical exciton energies are in the range of a few meV, or far less than the energies associated with the optical transitions of interest. Furthermore, in this first-order approach, the exciton energies are insensitive to strain. The exciton energies for a few representative quantum dots are shown in Table 2. As expected, the values are much smaller than the energies reported by previous investigators who studied unrealistically small quantum dots.

4. Effect of nanoindentation on optical properties

A simple approach is adopted to predict the effects of nanoindentation strain on the optical response of the self-assembled quantum dot array shown in Fig. 1. The microscope tip is treated as a cylindrical flat indenter, as shown in Fig. 7. In the experiment, the indenter surface is smooth and flat by design since in the process of tapering the fiber it is pulled until it fails by brittle cleavage fracture.

The contact between the tip and the surface is modeled using Hertzian elastic theory. To calculate the strain induced potential field, the full tensor strain field must be

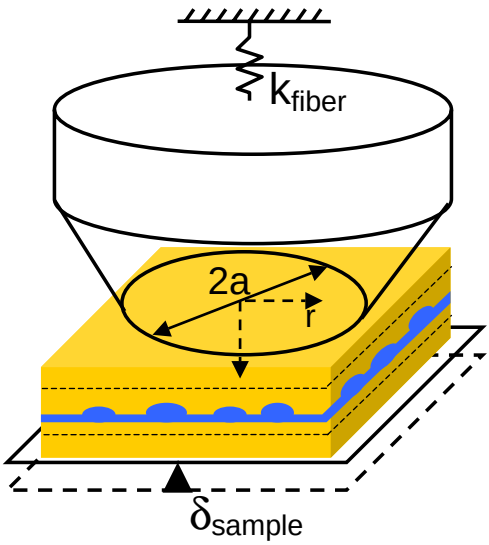

Fig. 7. Schematic of the indenter/sample mechanical interaction (not to scale). The sample stage is displaced vertically toward the tapered cylindrical indenter with aperture diameter $2a$. The displacement is accommodated by the compliance of the sample (indentation) and the compliance of the long optical fiber tip.

considered, so the friction-free indenter solution of Sneddon (1946) is adopted. With respect to the coordinate system shown in Fig. 7, the stress tensor components for an indentation depth ε and indenter radius a are derived by Sneddon (1946) as

$$\sigma_z = -\frac{4\mu(\lambda+\mu)}{\lambda+2\mu}\frac{\varepsilon}{\pi a}(J_1^0+\zeta J_2^0),$$

$$\tau_{zr} = -\frac{4\mu(\lambda+\mu)}{\lambda+2\mu}\frac{\varepsilon}{\pi a}\zeta J_2^1,$$

$$\sigma_\theta = -\frac{4\lambda\mu}{\lambda+2\mu}\frac{\varepsilon}{\pi a}J_1^0 - \frac{4\mu^2}{\rho(\lambda+2\mu)}\frac{\varepsilon}{\pi a}\left(J_1^0 - \frac{\lambda+\mu}{\mu}\zeta J_2^1\right), \tag{7}$$

where the integral J_n^m contains the cylindrical Bessel function J_m and is given by,

$$J_n^m = \int_0^\infty p^{n-1}\sin(p)\exp(-p\zeta)J_m(p\rho)\,\mathrm{d}p. \tag{8}$$

From these components, the strain field is computed for a given indentation depth ε. In computing the strain, it is assumed here for simplicity that the elastic constants λ and μ of the multiple layers of $In_{0.55}Al_{0.45}As$ and $Al_{0.35}Ga_{0.65}As$ are equal. The indentation depth ε is inferred as follows from the experimental sample stage displacement. The compliance of the long optical fiber tip contributes a significant fraction of the total sample stage displacement. The SiO_2 fiber is 750 μm in length, tapered from 5 μm in

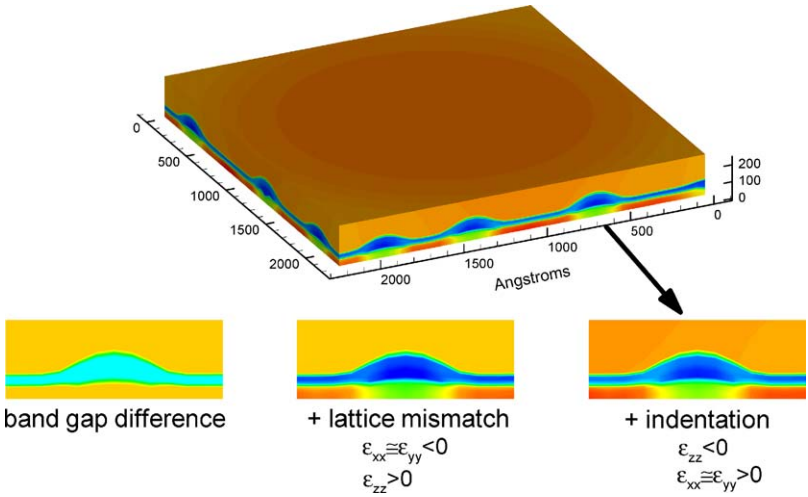

Fig. 8. Confining potential profile for heavy holes in the quantum dot array subjected to indentation. The cylindrical symmetry of the indenter can be seen in the potential along the top surface of the mesh. The total potential is due to the uniform composition effects, the lattice mismatch strain, and the indentation strain that is of opposite sign in the quantum dot layer.

width down to an aperture size of 250 nm. Based on a one-dimensional analysis it is straightforward to show that approximately 95 percent of the total system compliance is in the optical fiber tip. So through the experimental displacement range of 20 nm, the sample surface indentation depth ε is only 0.95 nm.

With this estimate for the range of indentation depths ε, the strain-induced deformation potential is computed from Eq. (4) for any arbitrary indentation depth, with the implicit assumption that the material behavior remains elastic. The potential profile for a sample stage displacement of 20 nm (penetration of 0.95 nm) is shown in Fig. 8. The potential field varies significantly from the unindented case and bears the cylindrical symmetry of the indenter. Fig. 8 also shows the contribution of the lattice mismatch strain to the overlap potential profile. It is interesting to note that to a first approximation, the nature of the indentation strain offsets the effects of the lattice mismatch strain in the material. However, both sources result in significant strain nonuniformity: the lattice mismatch is nonuniform on the length scale of the individual dots; and the indentation is nonuniform on the length scale of the array.

Electron and hole wave functions and energy levels are computed using potential profiles perturbed by indentation corresponding to sample displacement from 0 to 20 nm. From these states, optical spectra are evaluated according to the method described in the previous sections. Overlap plots of the kind shown in Fig. 5 are constructed to visualize the effect of strain on the optical spectra. Fig. 9 shows an overlap plot for the case of 20 nm sample displacement. Several key features are apparent in the plot.

First, both the electron and hole states present in the array shift to higher energies. This shift leads to a blue shift in the optical emission/absorption spectrum (shown in

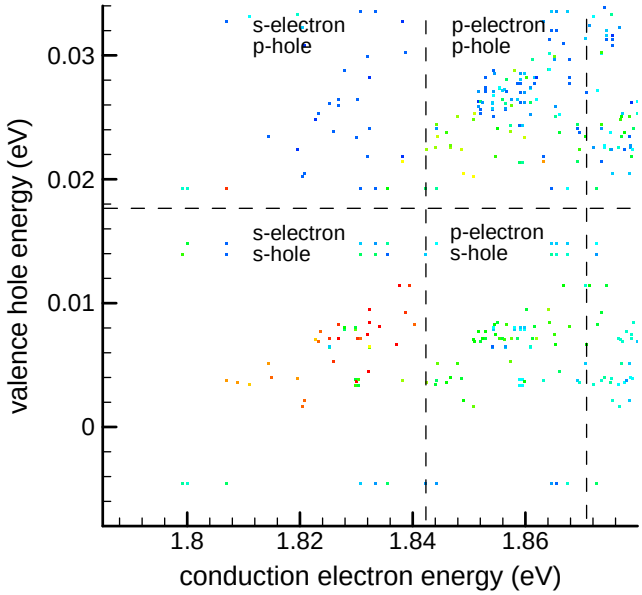

Fig. 9. Overlap diagram for electron and heavy hole states in the indented quantum dot array. The overlap shows much less structure than in the un-indented case (shown in Fig. 5 for the same energy range). Electron/hole transitions are reordered and spread in energy due to the shallow confinement of the heavy holes and the nonuniform applied strain. There is a positive shift in energy in both the conduction and valence bands.

Fig. 10) relative to the unindented case (shown in Fig. 6). A second observation is that ordering is lost between the electron and hole states, so the overlap diagram loses structure. A primary reason for this is the significantly shallower potential well for holes than for electrons. In the shallower potential well, the hole energies are more strongly shifted due to the indentation strain. The electron/hole strain effect asymmetry can be best visualized by noting the change in slope of the s-electron/s-hole overlap streak between the 0 nm case (Fig. 5) and the 20 nm case (Fig. 9). The indentation strain causes a shift in the hole energy that is approximately twice the shift per unit energy shift of the corresponding electron state than is shown in Fig. 5 for the unindented case. Additional disorder is induced in the overlap diagram due to the spatially varying strain field associated with indentation. The indentation induces a larger energy shift in dots near the indenter axis, for example. This effect is shown in Fig. 11, which plots the emission/absorption energy shift in a quantum dot as a function of dot position relative to the indenter axis.

By tracking the emission/absorption spectra of individual dots in the array over the range of sample displacements measured experimentally, a direct comparison is made between the model presented here and the experimental data. The result, for six representative dots in the model array, is shown in Fig. 12 plotted against data collected by Robinson et al. (1998). There are several striking differences between the

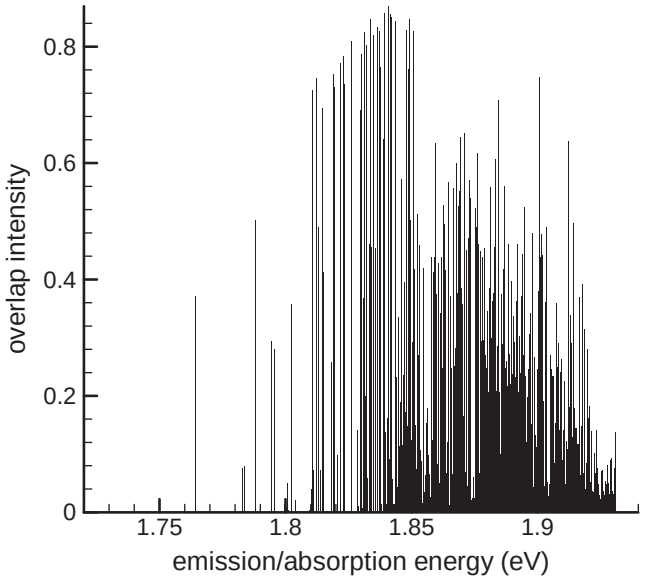

Fig. 10. Simulated emission/absorption spectrum for the indented array. The spectrum is similar to the un-indented case shown in Fig. 6, but there is a positive shift in energy and additional broadening due to the nonuniform indentation strain.

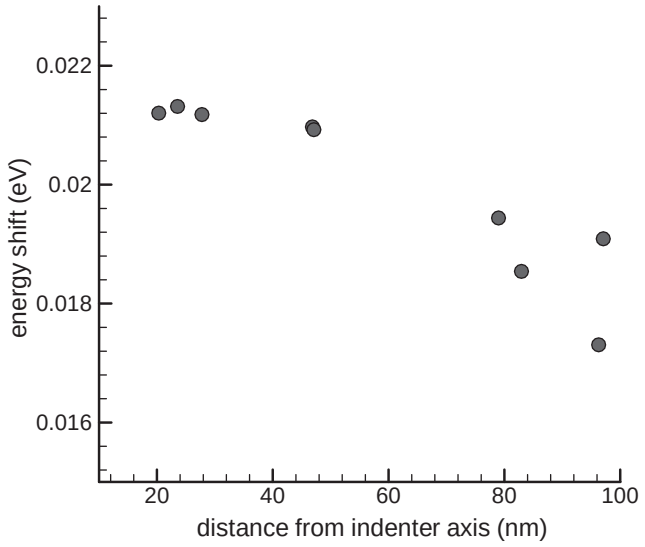

Fig. 11. Quantum dot photoemission/absorption shift as a function of distance from the axis of the indenter. The shift is a scalar function of the elastic indentation strain tensor, the magnitude of which is largest directly beneath the indenter. Variation in quantum dot size causes some variability in the energy shift.

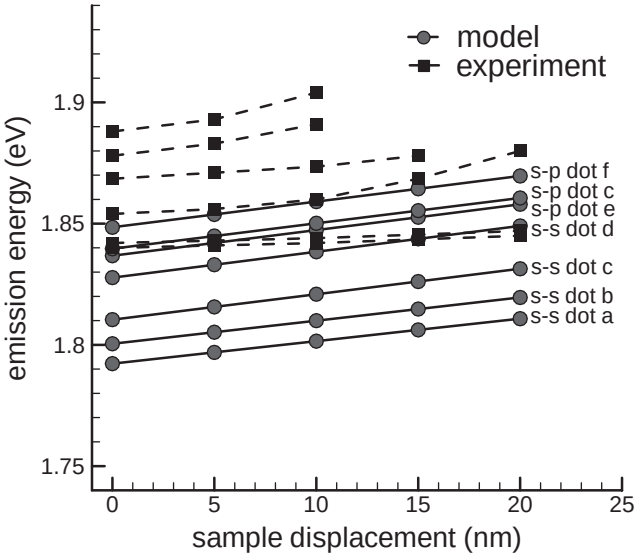

Fig. 12. Optical transition energy shift as a function of sample displacement for a sample of simulated and experimentally measured quantum dots. The magnitude of the computed energy shift is in reasonable agreement with the measured values, although the variation from dot to dot is not captured well. The three highest energy transitions computed here are between s-hole and p-electron states.

computed and experimentally measured data. First, the computed energies are in an energy range approximately 50 meV lower than the measured energies. This is likely due to discrepancies between material properties used in the calculation and actual material properties in the experimental material, particularly in the bandgap energies. No parameters in the computational model are fit to details of the experiment, so the relative agreement based on previously tabulated material properties is in fact quite good. Second, the energy shift in individual dots in the model is relatively (though not exactly) uniform and linear over the range of displacements studied, while the experimental energy shift varies from dot to dot and is generally nonlinear. This may be explained by noting that the actual applied indentation strain is likely not as uniform as assumed in the model; sources of nonuniformity include off-angle indentation or surface irregularities in the indenter or sample. Third, in the experimental data, several quantum dots cease to emit light in the energy range of interest. Possible explanations include (i) that a large nonuniform strain leads to the delocalization of hole states, or (ii) that the presence of electrically active dislocations dramatically changes the electrostatic potential landscape. The latter mechanism is discussed in the following section.

5. Dislocation nucleation in nanoindentation of buried quantum dot arrays

The electronic properties of nanometer scale semiconductor structures are highly sensitive to the presence of crystalline defects. The strong local electronic properties

of a single dislocation may render a quantum dot optically inactive. The electronic signature of a dislocation is dominated by two features: the local elastic strain field, which changes the effective potential experienced by an electron; and charging of unsatisfied covalent bonds, which contributes an additional electrostatic component to the potential experienced by an electron (Read, 1954). The latter effect, due to charging of dangling bonds, is temperature dependent and sensitive to the precise core structure of the dislocation. For these reasons dislocations are considered to be unacceptable in most nanoscale semiconductor devices and are avoided by design.

The view is adopted here that a single edge dislocation threading through an embedded quantum dot could affect the electron confining potential strongly enough to quench photoemission. This is suggested as a possible explanation for the observed quenching behavior in some of the dots measured by Robinson et al. (1998). It can be justified approximately by comparing the potential associated with the charging effect of the dislocation core, which can be significantly larger than the elastic strain effect, to the confinement energy scale for an electron in a single quantum dot. In the simplest approximation, the dislocation line induces an electrostatic potential proportional to the linear charge density λ, given by

$$\lambda = \frac{nq}{h}, \tag{9}$$

where n/h is the number n of electrons trapped along the dislocation core per length h. It is assumed that in this case electrostatic screening by other free charge is negligible since the material is undoped. Thus, the potential decays logarithmically with distance r from the dislocation, and can be written as

$$V = \frac{\lambda}{4\pi\varepsilon_0} \ln(r_0/r), \tag{10}$$

where ε_0 is the dielectric constant of the material and r_0 is a position near the dislocation core taken for comparison to the position of an electron test charge. Based on the assumption that the optical excitation of the material promotes valence electrons into the dangling bond states associated with the dislocation core, the fractional filling will approach one, as it does in a heavily doped material. With small corrections for the precise core structure of the dislocation and other effects such as temperature, the electrostatic potential V can vary by an amount on the order of the bandgap energy for an electron moving within the quantum dot array. For example, if the dislocation core traps one charge per nm of length, and if the dielectric constant of the film material is 10 relative to the permittivity of free space, the potential difference as a free electron moves from 5 to 50 nm away from the core is -0.33 eV, which would be sufficient to dramatically alter the potential profile that is otherwise controlled by strain and material properties.

The other contribution to the dislocation induced potential, from the elastic strain field of the dislocation, decays as $1/r$ with distance r from the dislocation core. The strain induced potential associated with a pure edge dislocation has a positive/negative asymmetry across the dislocation line due to the tensile/compressive nature of the dislocation elastic strain field. So while there is a spatial nonuniformity in the dislocation potential due to strain, in the simplest case the strain induced portion of the potential

decays more quickly than the electrostatic contribution and leads to no net shift of the confining potential.

Using standard Hertzian elastic contact theory, a simple estimate is developed to predict the depth to which a nanoindenter would have to penetrate before a dislocation would be expected to nucleate in the sample. In this framework, one would expect dislocation activity once penetration exceeds a critical depth, and in the view adopted here, quenching of photoemission in at least a subset of the quantum dots in the sample would then be expected. The nucleation estimate is based on a criterion similar to that of a fracture analysis of Rice and Thomson (1974), developed by Shenoy et al. (2000) for plane strain indentation, as follows.

For the case of a rigid flat axisymmetric indenter of diameter $2a$, dislocation nucleation is considered possible when the indenter displaces the sample surface a critical distance ε or greater. The critical depth ε is found by considering the force balance on a prismatic loop nucleating at a depth d_0 below the surface. The force tending to pull the dislocation loop out to the surface is due to the dislocation image field. For the case of a pair of infinite parallel edge dislocations (plane strain) the image force is given by Shenoy et al. (2000) as

$$f_{\text{up}} = \frac{b}{4\pi}\frac{2\mu(\lambda+\mu)}{(\lambda+2\mu)}\left(\frac{a^6+3d_0^2a^4+6d_0^4a^2}{(d_0^2+a^2)^3}\right), \tag{11}$$

where b is the Burgers displacement, and μ and λ are the Lamé elastic constants. For the axisymmetric case the term containing the depth d_0 and the diameter a will differ by a factor of order one. It can be assumed that as the ratio a/d_0 increases, the image forces for the axisymmetric case approach the plane strain result. The competing force, tending to push the dislocations into the sample, is due to the stress field of the indenter. The full field elasticity solution to the axisymmetric problem is due to Sneddon (1946); the driving force is given by

$$f_{\text{down}} = \frac{-\sqrt{2}\mu(\lambda+\mu)}{(\lambda+2\mu)}\frac{\varepsilon}{\pi a}\sqrt{\frac{a}{d_0}}. \tag{12}$$

When the competing forces balance at a reasonable dislocation depth d_0, typically taken as a single Burgers distance b, the critical depth ε can be found. An additional contribution to the energetics of dislocation nucleation, due to the formation of a surface step along the indenter edge, is neglected here. Shenoy et al. (2000) give the expression for the step energy correction for the plane strain case. In the limit that $a \gg d_0$, as is the case for the indenter/sample system under consideration, ε is given to within a constant of order one by

$$\varepsilon \cong b\sqrt{\frac{a}{d_0}}. \tag{13}$$

For the $Al_{0.35}Ga_{0.65}As$ matrix material surrounding the quantum dot array, the crude estimate for ε is approximately 5 nm. In the experiments performed by Robinson et al.

(1998), optical emission is quenched at a sample displacement of 10 to 20 nm, which corresponds to an indentation depth of approximately 1 nm. The nucleation criterion model assumes that the variation in elastic properties between the capping material and the dot material does not affect the elastic fields, and it ignores atomic scale features of the indenter. This simple estimate shows it is plausible, nevertheless, that the indentation is deep enough to approach the point at which dislocation nucleation is energetically favored. The details of this problem are currently under investigation.

6. Summary and conclusions

The effect of nanoindentation on the optical spectral properties of a self-assembled quantum dot array is well-described using a single-electron Hamiltonian approach with strain accounted for using deformation potential theory. It must be emphasized that while atomistic electronic structure approaches more accurately predict details of individual dot spectra, the simple model used here is the only computationally viable way to consider the coupled mechanics/physics problem for an entire array of quantum dots. Furthermore, by using as a model geometry the results from a morphology simulation, the problem of indentation on a quantum dot array can be simulated in a complete sense without recourse to parameter fitting based on any data specific to the experiments of interest.

The predicted optical spectra and indentation strain effect on the optical spectra agree well with the experimental results of Robinson et al. (1998). In particular, while the experimental and computed optical transition energy range is in disagreement by a small amount due to the initial choice of bandgap energies in the model, the *differences* between transition energies agree closely. And although the effects of nonuniform indentation strain were not considered in the model, the relatively uniform shift predicted by the model agrees quite satisfactorily with the average shift observed experimentally. This is encouraging given the order-of-magnitude discrepancy between the measured shift and the initial estimates made by Robinson et al. (1998) based on simple one-dimensional mechanics. It is important to note, also, that the strain effect over the range of indentation considered here is not necessarily linear, due both to the difference in confinement energies for the electrons and holes in the material as well as the observed delocalized states that occur at higher energies.

The small and relatively size- and strain-insensitive value of the exciton binding energy for the quantum dots is an important conclusion. For a representative sample of quantum dots in the array, the exciton binding energy was nearly constant at approximately 6 meV, which is small relative to the confinement energy scale of roughly 0.5–1.0 eV. The exciton energy can be viewed as a second-order shift in the optical transition energies due to the Coulomb interaction energy of the electron/hole pair. But for dots of this realistic 20 nm size, the small shift is nearly negligible when compared with the uncertainty in the bandgap energy, for example.

Finally, the justification of the possibility of dislocation quenching effects is a key result that has not been considered in the literature on strained quantum dots. The crude

estimate of the indentation depth required to nucleate a dislocation gives an argument for the possible presence of dislocations on continued indentation. Based on simple electrostatic arguments, the perturbation due to charging of a dislocation core can then be shown to be on the order of the confinement energy scale. This would strongly affect the spectrum of electron and hole states in the material and could arguably "quench" the photoemission and absorption properties of individual dots.

Acknowledgements

The support of National Science Foundation CAREER Award No. CMS 02-96102 is gratefully acknowledged. The authors thank Prof. Bennett Goldberg of Boston University for many helpful discussions.

References

Bimberg, D., Grundmann, M., Ledentsov, N.N., 1999. Quantum Dot Heterostructures. Wiley, London.

Biolatti, E., Iotti, R.C., Zanardi, P., Rossi, F., 2000. Quantum information processing with semiconductor macroatoms. Phys. Rev. Lett. 85, p5647–5650.

Davies, J.H., 1998. The Physics of Low-dimensional Semiconductors.. Cambridge University Press, Cambridge.

Grundmann, M., Stier, O., Bimberg, D., 1995. InAs/GaAs pyramidal quantum dots: strain distribution, optical phonons, and electronic structure. Phys. Rev. B 52, 11969–11981.

Jiang, H., Singh, J., 1997. Strain distribution and electronic spectra of InAs/GaAs self-assembled dot: an eight-band study. Phys. Rev. B 56, 4696–4701.

Johnson, H.T., Freund, L.B., 2001. The influence of strain on confined electronic states in semiconductor quantum structures. Int. J. Sol. Struc. 38, 1045–1062.

Johnson, H.T., Nguyen, V., Bower, A.F., 2002. Simulated self-assembly and optoelectronic properties of InAs/GaAs quantum dot arrays. J. Appl. Phys. 92, 4653–4663.

Johnson, H.T., Bose, R., Goldberg, B.B., Robinson, H.D., 2003. Simulation evidence for lateral excitation transfer in a self-assembled quantum dot array. Appl. Phys. Lett. 82, 3382–3384.

Johnson, H.T., Freund, L.B., Akyuž, C.D., Zoolavsky, A., 1998. Finite element analysis of strain effects on electronic and transport properties in quantum dots and wires. J. Appl. Phys. 84, 3714–3725.

Leon, R., Fafard, S., Leonard, D., Merz, J.L., Petroff, P.M., 1995. Visible luminescence from semiconductor quantum dots in large ensembles. Appl. Phys. Lett. 67, 521–523.

Pryor, C., 1998. Quantum wires formed from coupled InAs/GaAs strained quantum dots. Phys. Rev. Lett. 80, 3579–3581.

Pryor, C., 1998a. Eight-band calculations of strained InAs/GaAs quantum dots compared with one-, four-, and six-band approximations. Phys. Rev. B 57, 7190–7195.

Read, W.T., 1954. Theory of dislocations in germanium. Philos. Mag. 45, 775–796.

Rice, J.R., Thomson, R., 1974. Ductile versus brittle behavior of crystals. Philos. Mag. 29, 73–97.

Robinson, H.D., Muller, M.G., Goldberg, B.B., Merz, J.L., 1998. Local optical spectroscopy of self-assembled quantum dots using a near-field optical fiber probe to induce a localized strain field. Appl. Phys. Lett. 72, 2081–2083.

Robinson, H.D., Goldberg, B.B., Merz, J.L., 2001. Observation of excitation transfer among neighboring quantum dots. Phys. Rev. B 64, 075308.

Shenoy, V.B., Phillips, R., Tadmor, E.B., 2000. Nucleation of dislocations beneath a plan strain indenter. J. Mech. Phys. Sol. 48, 649–673.

Singh, J., 1993. Physics of Semiconductors and Their Heterostructures. McGraw-Hill, Inc., New York.

Sneddon, I., 1946. Boussinesq's problem for a flat-ended cylinder. Proc. Camb. Philos. Soc. 42, 29–39.

Winter, J.O., Liu, T.Y., Korgel, B.A., Schmidt, C.E., 2001. Recognition molecule directed interfacing between semiconductor quantum dots and nerve cells. Adv. Mater. 13, 1673–1677.

Zhang, Y., Bower, A.F., 1999. Numerical simulations of island formation in a coherent strained epitaxial thin film system. J. Mech. Phys. Sol. 47, 2273–2297.

Zunger, A., 2001. Pseudopotential theory of semiconductor quantum dots. Phys. Stat. Sol. B 224, 727–734.